The numerical simulation of ship waves using cartesian-grid and volume-of-fluid methods

Douglas G. Dommermuth[1], Thomas T. O'Shea[1], Donald C. Wyatt[1],
Mark Sussman[2], Gabriel D. Weymouth[3], Dick K.P. Yue[3],
Paul Adams[4], and Randall Hand[4]

[1]Naval Hydrodynamics Division, Science Applications International Corporation,
10260 Campus Point Drive, MS 35, San Diego, CA 92121

[2]Department of Mathematics, Florida State University, Tallahassee, FL 32306

[3]Department of Mechanical Engineering, Massachusetts Institute of Technology, Cambridge, MA 02139

[4]U.S. Army Engineer Research and Development Center, Vicksburg, MS 39180

Abstract

Numerical predictions are compared to experimental measurements of ship models moving with forward speed, including model 5415 and model 5365 (Athena). The ability to model forced-motions is illustrated using a heaving sphere moving with forward speed.

Introduction

The Numerical Flow Analysis (NFA) code provides turnkey capabilities to model breaking waves around a ship, including both plunging and spilling breaking waves, the formation of spray, and the entrainment of air. NFA uses a cartesian-grid formulation with immersed-body and volume-of-fluid (VOF) methods. The governing equations are formulated on a cartesian grid thereby eliminating complications associated with body-fitted grids. The sole geometric input into NFA is a surface panelization of the ship hull. No additional gridding beyond what is already used in potential-flow methods and hydrostatics calculations is required. The ease of input in combination with a flow solver that is implemented using parallel-computing methods permit the rapid turn around of numerical simulations of complex interactions between free surfaces and ships.

Based on Colella, Graves, Modiano, Puckett & Sussman (1999), free-slip boundary conditions are imposed on the surface of the ship hull. The fractional areas and volumes of very small cells are merged to improve the conditioning of the Poission solver (Mampaey & Xu 1995). The grid is stretched along the cartesian axes using one-dimensional elliptic equations to improve resolution near the ship hull and the free-surface interface. Away from the ship and the free-surface interface, where the flow is less complicated, the mesh is coarser. Details of the grid stretching algorithm, which uses weight functions that are specified in physical space, are provided in

Knupp & Steinerg (1993). Free-slip boundary conditions are also imposed at the entrance, along the sides, and at the top and bottom of the computational domain. At the exit, Orlanski-like boundary conditions are imposed (Orlanski 1976).

The VOF portion of the numerical algorithm is used to track the free-surface interface, including the large-scale effects of breaking waves, spray formation and air entrainment. A novel regridding scheme is introduced whereby the level of water at the entrance of the computational domain is preserved. The interface tracking of the free surface is second-order accurate in space and time. At each time step, the position of the free surface is reconstructed using piece-wise planar surfaces (Rider, Kothe, Mosso, Cerutti & Hochstein 1994, Gueyffier, Li, Nadim, Scardovelli & Zaleski 1999). The advection portion of the VOF algorithm uses an operator-split method (Puckett, Almgren, Bell, Marcus & Rider 1997). The advection algorithm implements a correction to improve mass conservation when the flow is not solenodal due to numerical errors.

The convective terms in the momentum equations are treated using a slope-limited, third-order QUICK scheme as discussed in Leonard (1997). A Smagorinsky turbulence model is also implemented.. There are no special treatments required to model either the flow separation at the transom or the wave overturning at the bow. A second-order, variable-coefficient Poisson equation is used project the velocity onto a solenoidal field. A pre-conditioned conjugate-gradient method is used to solve the Poisson equation.

NFA is written in Fortran 90. The governing equations are solved using a domain decomposition method. The domains are distributed over the nodes of a parallel computer. Communication between processors on the Cray XT3 and X1 is performed using either Crays shared memory access library (SHMEM) or MPI. The CPU requirements are linearly proportional to the number of

grid points and inversely proportional to the number of processors. For the most part, NFA performed equally well on the Cray X1, which is a vector machine, and the Cray XT3, which is a massively parallel machine. The main exception involved portions of NFA that involved conditional statements that could not be vectorized on the Cray X1. Together, the ease of input and usage, the ability to model and resolve complex free-surface phenomena, and the speed of the numerical algorithm provide a robust capability for simulating the free-surface disturbances near a ship.

Formulation

Consider turbulent flow at the interface between air and water. Let u_i denote the three-dimensional velocity field as a function of space (x_i) and time (t). The coordinate system is fixed with respect to the ship. v_i is the velocity of the ship. v_i includes the effects of rigid-body translation and rigid-body rotation. For an incompressible flow, the conservation of mass gives

$$\frac{\partial u_i}{\partial x_i} = 0 \ . \tag{1}$$

u_i and x_i are normalized by U_o and L_o, which denote the free-stream velocity and the length of the body, respectively.

Following a procedure that is similar to Rider et al. (1994), we let ϕ denote the fraction of fluid that is inside a cell. By definition, $\phi = 0$ for a cell that is totally filled with air, and $\phi = 1$ for a cell that is totally filled with water.

The convection of ϕ is expressed as follows:

$$\frac{\partial \phi}{\partial t} + \frac{\partial}{\partial x_j}\left[(u_i - v_i)\phi\right] = \frac{\partial Q}{\partial x_j} \ , \tag{2}$$

v_i is the velocity of the body. The coordinate system is fixed with respect to the body (Repetto 2000). Q is a sub-grid-scale flux which can model the entrainment of gas into the liquid. Dommermuth, Innis, Luth, Novikov, Schlageter & Talcott (1998) provide details of a sub-grid model that is appropriate for interface capturing methods that allow mixing of air and water. Since the present formulation maintains a sharp interface, $Q = 0$.

Let ρ_ℓ and μ_ℓ respectively denote the density and dynamic viscosity of water. Similarly, ρ_g and μ_g are the corresponding properties of air. The flows in the water and the air are governed by the Navier-Stokes equations:

$$\frac{du_i}{dt} + \frac{\partial}{\partial x_j}\left[(u_i - v_i)u_j\right] = -\frac{1}{\rho}\frac{\partial P}{\partial x_i}$$
$$+\frac{1}{\rho R_e}\frac{\partial}{\partial x_j}\left(2\mu S_{ij}\right) - \frac{G_i}{F_r^2} + \frac{\partial \tau_{ij}}{\partial x_j} \ , \tag{3}$$

where $R_e = \rho_\ell U_o L_o / \mu_\ell$ is the Reynolds number and $F_r^2 = U_o^2/(gL_o)$ is the Froude number. g is the acceleration of gravity. G_i is a body force that rotates with the body (Repetto 2000). P is the pressure. As described in Dommermuth et al. (1998), τ_{ij} is the subgrid-scale stress tensor. S_{ij} is the deformation tensor:

$$S_{ij} \quad = \quad \frac{1}{2}\left(\frac{\partial u_i}{\partial x_j} + \frac{\partial u_j}{\partial x_i}\right) \ . \tag{4}$$

ρ and μ are respectively the dimensionless variable densities and viscosities:

$$\begin{aligned}\rho(\phi) &= \lambda + (1-\lambda)\mathrm{H}(\phi)\\ \mu(\phi) &= \eta + (1-\eta)\mathrm{H}(\phi) \ ,\end{aligned} \tag{5}$$

where $\lambda = \rho_g/\rho_\ell$ and $\eta = \mu_g/\mu_\ell$ are the density and viscosity ratios between air and water. For a sharp interface, with no mixing of air and water, H is a step function. In practice, a mollified step function is used to provide a smooth transition between air and water.

A no-flux condition is imposed on the surface of the ship hull:

$$u_i n_i = v_i n_i \tag{6}$$

where n_i denotes the normal to the ship hull that points into the fluid.

As discussed in Dommermuth et al. (1998), the divergence of the momentum equations (3) in combination with the conservation of mass (1) provides a Poisson equation for the dynamic pressure:

$$\frac{\partial}{\partial x_i}\frac{1}{\rho}\frac{\partial P}{\partial x_i} = \Sigma \ , \tag{7}$$

where Σ is a source term. As shown in the next section, the pressure is used to project the velocity onto a solenoidal field.

NUMERICAL TIME INTEGRATION

Based on Sussman (2003a), a second-order Runge-Kutta scheme is used to integrate with respect to time the field equations for the velocity field. Here, we illustrate how a volume of fluid formulation is used to advance the volume-fraction function Similar examples are provided by Rider et al. (1994). During the first stage of the Runge-Kutta algorithm, a Poisson equation for the pressure is solved:

$$\frac{\partial}{\partial x_i}\frac{1}{\rho(\phi^k)}\frac{\partial P^*}{\partial x_i} = \frac{\partial}{\partial x_i}\left(\frac{u_i^k}{\Delta t} + R_i\right) \ , \tag{8}$$

where R_i denotes the nonlinear convective, hydrostatic, viscous, sub-grid-scale, and body-force terms in the momentum equations. u_i^k and ρ^k are respectively the velocity components at time step k. Δt is the time step. P^* is the first prediction for the pressure field.

For the next step, this pressure is used to project the velocity onto a solenoidal field. The first prediction for the velocity field (u_i^*) is

$$u_i^* = u_i^k + \Delta t \left(R_i - \frac{1}{\rho(\phi^k)} \frac{\partial P^*}{\partial x_i} \right) \qquad (9)$$

The volume fraction is advanced using a volume of fluid operator (VOF):

$$\phi^* = \phi^k - \text{VOF}\left(u_i^k, \phi^k, \Delta t\right) \qquad (10)$$

Details of the VOF operator are provided later. A Poisson equation for the pressure is solved again during the second stage of the Runge-Kutta algorithm:

$$\frac{\partial}{\partial x_i} \frac{1}{\rho(\phi^*)} \frac{\partial P^{k+1}}{\partial x_i} = \frac{\partial}{\partial x_i} \left(\frac{u_i^* + u_i^k}{\Delta t} + R_i \right) \qquad (11)$$

u_i is advanced to the next step to complete one cycle of the Runge-Kutta algorithm:

$$u_i^{k+1} = \frac{1}{2} \left(u_i^* + u_i^k + \Delta t \left(R_i - \frac{1}{\rho(\phi^*)} \frac{\partial P^{k+1}}{\partial x_i} \right) \right) \quad , (12)$$

and the volume fraction is advanced to complete the algorithm:

$$\phi^{k+1} = \phi^k - \text{VOF}\left(\frac{u_i^* + u_i^k}{2}, \phi^k, \Delta t \right) \qquad (13)$$

GRIDDING

Along the cartesian axes, one-dimensional stretching is performed using a differential equation. Let x denote the position of the grid points in physical space, and let ξ denote the position of the grid points in a mapped space. As shown by Knupp & Steinerg (1993), the differential equation that describes grid stretching in one dimension is as follows:

$$\frac{\partial^2 x}{\partial \xi^2} + \frac{1}{w} \frac{\partial w}{\partial \xi} \frac{\partial x}{\partial \xi} = 0 \quad , \qquad (14)$$

where $w(x)$ is a weight function that is specified in physical space. For example, suppose the grid spacing is constant but different for $x < x_o$ and $x > x_1$. Between $x_o \leq x \leq x_1$, there is a transition zone from one grid spacing to the next. Then the following weight function may be used to describe this distribution of grid points:

$$
\begin{aligned}
w(x) &= w_0 \text{ for } x < x_0 \\
w(x) &= \frac{w_0 - w_1}{2} \left(1 + \cos(\frac{\pi(x - x_0)}{x_1 - x_0}) \right) \\
&+ w_1 \text{ for } x_0 \leq x \leq x_1 \\
w(x) &= w_1 \text{ for } x > x_1 \quad .
\end{aligned}
\qquad (15)
$$

Using this approach, multiple zones of grid clustering may be specified. For example, along the x-axis (x_1 in indical notation), grid points may be clustered near the bow and stern. For the y-axis (x_2 in indical notation), grid points are clustered near the centerline out beyond the half beam. Finally, for the z-axis (x_3 in indical notation), grid points are clustered near the mean waterline in a region that is between the top and bottom of the ship hull. Note that equation 14, is a nonlinear equation that is solved iteratively.

ENFORCEMENT OF BODY BOUNDARY CONDITIONS

A no-flux boundary condition is imposed on the surface of the body using a finite-volume technique. A signed distance function ψ is used to represent the body. ψ is positive outside the body and negative inside the body. The magnitude of ψ is the minimal distance between the position of ψ and the surface of the body. ψ is zero on the surface of the body. ψ is calculated using a surface panelization of the hull form. Green's theorem is used to indicate whether a point is inside or outside the body, and then the shortest distance from the point to the surface of the body is calculated. Triangular panels are used to discretize the surface of the body. The shortest distance to the surface of the body can occur on either a surface, edge, or vertice of a triangular panel. Details associated with the calculation of ψ are provided in Sussman & Dommermuth (2001).

Cells near the ship hull may have an irregular shape, depending on how the surface of the ship hull cuts the cell. On these irregular boundaries, the finite-volume approach is used to impose free-slip boundary conditions. Let S_b denote the portion of the cell whose surface is on the body, and let S_o denote the other bounding surfaces of the cell that are not on the body. Gauss's theorem is applied to the volume integral of equation 8:

$$\int_{S_o + S_b} ds \frac{n_i}{\rho(\phi^k)} \frac{\partial P^*}{\partial x_i} = \int_{S_o + S_b} ds \left(\frac{u_i^k n_i}{\Delta t} + R_i n_i \right) \quad . (16)$$

Here, n_i denotes the components of the unit normal on the surfaces that bound the cell. Based on equation 9, a Neumann condition is derived for the pressure on S_b as follows:

$$\frac{n_i}{\rho(\phi^k)} \frac{\partial P^*}{\partial x_i} = -\frac{u_i^* n_i}{\Delta t} + \frac{u_i^k n_i}{\Delta t} + R_i n_i \quad . \qquad (17)$$

The Neumann condition for the velocity (6) is substituted into the preceding equation to complete the Neumann condition for the pressure on S_b:

$$\frac{n_i}{\rho(\phi^k)} \frac{\partial P^*}{\partial x_i} = -\frac{v_i^* n_i}{\Delta t} + \frac{u_i^k n_i}{\Delta t} + R_i n_i \quad . \qquad (18)$$

3

This Neumann condition for the pressure is substituted into the integral formulation in equation 16:

$$\int_{S_o} ds \frac{1}{\rho(\phi^k)} \frac{\partial P^*}{\partial x_i} n_i = \int_{S_o} ds \left(\frac{u_i^k n_i}{\Delta t} + R_i n_i \right)$$
$$+ \int_{S_b} ds \frac{v_i^* n_i}{\Delta t} \quad (19)$$

This equation is solved using the method of fractional areas. Details associated with the calculation of the area fractions are provided in Sussman & Dommermuth (2001) along with additional references. Cells whose cut volume is less than 25% of the full volume of the cell are merged with neighbors. The merging occurs along the direction of the steepest gradient of the signed-distance function ψ. This improves the conditioning of the Poisson equation for the pressure. As a result, the stability of the projection operator for the velocity is also improved (see equations 9 and 12).

INTERFACE RECONSTRUCTION AND ADVECTION

In our VOF formulation, the free surface is reconstructed from the volume fractions using piece-wise linear polynomials. The reconstruction is based on algorithms that are described by Gueyffier et al. (1999). The surface normals are estimated using weighted central differencing of the volume fractions. A similar algorithm is described by Pilliod & Puckett (1997). Near the body, care must be taken to use cells whose volume fraction is exterior to the body in the calculation of the normal to the free-surface interface. The advection portion of the algorithm is operator split, and it is based on similar algorithms reported in Puckett et al. (1997). Major differences between the present algorithm and earlier methods include special treatments to account for the body and to alleviate mass-conservation errors due to the presence of non-solenoidal velocity fields.

Let F_i denote flux through the faces of a cell. F_i is expressed in terms of the relative velocity $(u_i - v_i)$ and the areas of the faces of the cell (A_i) that are cut by the ship hull:

$$F_i = A_i \left(u_i - v_i \right) \quad . \quad (20)$$

If the ship hull does not cut the cell, then A_i correspond to the surface areas that bound the cell. Near the ship hull, A_i is some fraction of the surface areas that bound the cell. Note that $A_i = 0$ inside the ship hull. Based on an application of Gauss's theorem to the volume integral of Equation 1 and making use of Equation 6:

$$F_i^+ - F_i^- = 0 \quad , \quad (21)$$

where F_i^+ is the flux on the positive i-th face of the cell and F_i^- is the flux on the negative i-th face of the cell.

Due to numerical errors, equation 21 is not necessarily satisfied. Let $\mathcal{E}$ denote the resulting numerical error for any given cell. For each cell whose flux is not conserved, a correction is applied prior to performing the VOF advection. For example, the following reassignment of the flux along the vertical direction ensures that the redefined flux is conserved:

$$\tilde{F}_3^+ = F_3^+ - \frac{\mathcal{E} A_3^+}{A_3^+ + A_3^-}$$
$$\tilde{F}_3^- = F_3^- + \frac{\mathcal{E} A_3^-}{A_3^+ + A_3^-} \quad (22)$$

Based on this new flux, new relative velocities are defined on the faces of the cell:

$$\hat{u}_i = \frac{\Delta x_i \tilde{F}_i}{V} \quad (23)$$

where Δx_i is the grid spacing and $V = \Delta x_1 \Delta x_2 \Delta x_3$ is the volume of the cell. Away from the ship hull, $\hat{u}_i$ is the relative velocity with a corrective term to conserve mass. Inside the ship hull, $\hat{u}_i = 0$ because $A_i = 0$. Near the ship hull, $\hat{u}_i$ is scaled by the fraction of area that is cut by the presence of the ship hull. $\hat{u}_i$ is continuous across the faces of the cells along $x-$ and $y-$axes, but discontinuous across the faces along the $z-$axis because in this particular example that is the axis where the flux has been corrected.

Equation 2 is operator split. A dilation term is added to ensure that the volume fraction remains between $0 \leq \phi \leq 1$ during each stage of the splitting (Puckett et al. 1997). The resulting discrete set of equations for the first stage of the time-stepping procedure is provided below:

$$\tilde{\phi} = \phi^k \quad - \quad \frac{\mathcal{F}_1 \left[\left(\hat{u}_1^+ \right)^k, \phi^k, \Delta t \right] - \mathcal{F}_1 \left[\left(\hat{u}_1^- \right)^k, \phi^k, \Delta t \right]}{V}$$
$$+ \quad \Delta t \tilde{\phi} \frac{\left(\hat{u}_1^+ \right)^k - \left(\hat{u}_1^- \right)^k}{\Delta x_1}$$
$$\tilde{\tilde{\phi}} = \tilde{\phi} \quad - \quad \frac{\mathcal{F}_2 \left[\left(\hat{u}_2^+ \right)^k, \tilde{\phi}, \Delta t \right] - \mathcal{F}_2 \left[\left(\hat{u}_2^- \right)^k, \tilde{\phi}, \Delta t \right]}{V}$$
$$+ \quad \Delta t \tilde{\tilde{\phi}} \frac{\left(\hat{u}_2^+ \right)^k - \left(\hat{u}_2^- \right)^k}{\Delta x_2}$$
$$\phi^* = \tilde{\tilde{\phi}} \quad - \quad \frac{\mathcal{F}_3 \left[\left(\hat{u}_3^+ \right)^k, \hat{\phi}, \Delta t \right] - \mathcal{F}_3 \left[\left(\hat{u}_3^- \right)^k, \hat{\phi}, \Delta t \right]}{V}$$
$$+ \quad \Delta t \tilde{\tilde{\phi}} \frac{\left(\hat{u}_3^+ \right)^k - \left(\hat{u}_3^- \right)^k}{\Delta x_3} \quad , \quad (24)$$

$\mathcal{F}_i$ denotes VOF advection based on the uncut areas of the faces of the cell. As an example, for a cell that is full of water, $\mathcal{F}_1(\hat{u}_1, \phi, \Delta t) = \phi \hat{u}_1 \Delta t \Delta x_2 \Delta x_3$. The dilation term is treated explicitly in the first two parts of the operator-slip algorithm and implicitly in the last part of

the preceding equation. Note that the order of the splitting is alternated from time step to time step to preserve second-order accuracy.

The free-surface interface that is reconstructed from the volume fractions is most often calculated and visualized using commercial codes. Specifically, commercial codes calculate the 0.5 isosurface of the volume-fraction function ϕ. The free-surface interface that is calculated from the 0.5 isosurface is different from the free-surface interface that is reconstructed from the volume fractions. To illustrate this point, consider a cell whose volume fraction ϕ_o is between half full and full, $0.5 \leq \phi_o \leq 1$. Let Δz denote the height of the cell. Assume that the free-surface interface is horizontal and that all the fluid is sitting in the bottom of the cell. Then the height of the free-surface interface above the bottom of the cell based on VOF reconstruction is as follows:

$$\eta = \phi_o \Delta z \ .\tag{25}$$

In contrast, based on the 0.5 isosurface, the height of the free-surface interface is

$$\eta = \left(\frac{3}{2} - \frac{1}{2\phi_o} \right) \ .\tag{26}$$

The maximum difference between equations 25 and 26 occurs when $\phi_o = 3/4$. The error at this point is about 11% higher for 0.5 isosurface relative to VOF reconstruction. If the volume fraction is less than $\phi < 0.5$, then the 0.5 isosurface does not even exist. This is problematic in visualizations of turbulent flows with lots of spray because droplets and sheets of water can suddenly appear and disappear.

RADIATION CONDITIONS

Exit boundary conditions are required in order to conserve mass and flux. For ships with forward speed, an Orlanski-like formulation (Orlanski 1976) provides the necessary radiation condition.

$$\frac{\partial u_1}{\partial t} + u_c \frac{\partial u_1}{\partial x} = 0 \ .\tag{27}$$

u_c is the forward speed of the ship, and u_1 is the water-particle velocity along the x-axis. For the other components of velocity and the volume fraction, zero gradients are imposed at the exit of the computational domain:

$$\frac{\partial u_2}{\partial x} = \frac{\partial u_3}{\partial x} = \frac{\partial \phi}{\partial x} = 0 \ .\tag{28}$$

Neumman conditions are specified for the pressure in a manner that is very similar to the imposition of free-slip conditions on the ship hull (see equations 16 thru 19). Based on the x-component of momentum,

$$\frac{1}{\rho} \frac{\partial P}{\partial x} = -\frac{\partial u_1}{\partial t} + R_1 \ .\tag{29}$$

Upon substitution of equation 27 into the preceding equation, the following Neumann condition is derived for the pressure at the exit of the computational domain:

$$\frac{1}{\rho} \frac{\partial P}{\partial x} = u_c \frac{\partial u_1}{\partial x} + R_1 \ .\tag{30}$$

This equation is substituted into the set of finite-volume equations that govern the pressure (see equation 19).

Equations 27 thru 30 prevent the reflection of disturbances back into the interior of the computational domain. However, these equations do not guarantee the conservation of mass. In order to conserve mass, a regridding procedure is introduced. The initial volume fraction is integrated for the grid cells that are on the leading edge of the computational domain. This integrated quantity is used to maintain a constant mean water level at the entrance to the computational domain. At the end of each time step, changes in the integrated volume fraction are calculated. Any changes in the integrated volume fraction are eliminated by imposing a vertical velocity that brings the mean water level at the leading edge back into alignment. The velocity correction is used to move the volume fractions over the entire computational domain either up or down, depending on the situation. A VOF method is used to move the volume fractions. The VOF method ensures that the free-surface interface remains sharp during the regridding process.

INITIAL TRANSIENTS

Initial transients are minimized using an adjustment procedure. An analysis of adjustment procedures as it applies to free-surface problems is provided in Dommermuth (1994) and Dommermuth (2000). Let $f(t)$ denote the adjustment factor as a function of time, then $f(t)$ and its derivative $f'(t)$ are by definition

$$\begin{aligned} f(t) &= 1 - \exp(-(\frac{t}{T_o})^2) \\ f'(t) &= 2\frac{t}{T_o^2} \exp(-(\frac{t}{T_o})^2) \ , \end{aligned}\tag{31}$$

where T_o is the adjustment time. The adjusted velocity of a ship moving with unit forward speed along the x-axis is

$$v_1 = f(t) \ .\tag{32}$$

For a ship hull that is oscillating up and down, the vertical motion (z) and vertical velocity (v_3) of the free surface in a body-fixed coordinate system are

$$\begin{aligned} z &= A sin(\omega t) f(t) \\ v_3 &= A\omega \cos(\omega t) f(t) + A sin(\omega t) f'(t) \ . \end{aligned}\tag{33}$$

A is the amplitude and ω is the frequency of the vertical motion. Since the free surface moves relative to the

ship hull, there is no need to recalculate how the ship hull intersects the cartesian grid. This is the major advantage of body-fixed coordinate systems relative to coordinate systems that are not fixed relative to the body (Repetto 2000). The main disadvantage of body-fixed coordinate systems is that for rotational modes of motion, the Courant condition may be very restrictive near the edges of the computational domain.

ENFORCEMENT OF COURANT CONDITIONS

The momentum equations are integrated in time using an explicit Runge-Kutta algorithm. As a result, a Courant condition must be enforced for the maximum relative velocity:

$$|u_i - v_i| \leq C \frac{\Delta x_i}{\Delta t} \tag{34}$$

C is a coefficient that ensures that the Courant condition is satisfied for both the momentum equations and the VOF advection. Typically, $C = 0.45$ in the numerical results that are presented in this paper. If the Courant condition is exceeded, the magnitude of the velocity is reduced such that the Courant condition is satisfied. This clipping of the velocity field tends to occur in regions where fine spray is formed, especially in the rooster-tail region.

TREATMENT OF CONVECTIVE TERMS

The convective terms in the momentum equations (see Equation 3) are calculated using a slope-limited, QUICK, finite-difference scheme (Leonard 1997). Special treatments are required near the ship hull. One possibility is to use one-sided differencing. However, one-sided differencing is often unstable. Another possibility is to extend the velocity of the fluid into the ship hull. In this case, setting the velocity equal to zero inside the body is stable, but too "sticky." Another possibility is to extend the fluid velocity into the ship hull in such a manner that the no-flux condition is met right at the ship hull. The interior flow that meets this condition is as follows:

$$u_i = (v_j n_j) n_i \quad , \tag{35}$$

where recall v_j is velocity of the body and n_i is the unit normal that points along gradient of the signed-distance function (ψ). At the ship hull, $u_i n_i = v_i n_i$ using this formulation of the interior flow.

DENSITY SMOOTHING

The density as a function of the volume fraction is smoothed using a three-point stencil (1/4,1/2,1/4) that is applied consecutively along each of the cartesian axes. This improves the conditioning of the Poisson equation (Equations 8 & 11). If the density is smoothed, then the same smoothed density must be used in the projection steps (Equations 9 & 12).

Results

5365 geometry

Experimental measurements of model 5365 have been performed at Froude numbers $Fr = 0.2518$ and 0.4316 that correspond to equivalent full-scale speeds of 10.5 and 18 knots, respectively. Details of the experimental measurements are provided in Wilson, Fu, Pence & Gorski (2006).

Corresponding to these experiments, three-dimensional numerical simulations using 680x192x128=16,711,680 grid points, 4x8x4=128 sub-domains, and 128 nodes have been performed on a Cray XT3. The length, width, depth, and height of the computational domain are respectively 3.0, 1.0, 1.0, 0.5 ship lengths (L). Grid stretching is employed in all directions. The smallest grid spacing is 0.002L near the ship and mean waterline, and the largest grid spacing is 0.02L in the far field. This provides about 8 x 61 cells across the transom of the low Froude-number case, and 11 x 61 grid cells for the high Froude-number case. For the low Froude-number case, there are 200 cells per transverse wavelength (0.398L) where the grid spacing is fine and 20 grid cells where it is coarse. For the high Froude-number case, there are 585 cells per transverse wavelength (1.17L) where the grid spacing is fine and 58.5 grid cells where it is coarse. Initial transients are minimized by slowly ramping up the free-stream current. The period of adjustment associated with this ramp up is 0.5 in non-dimensional units of time, where $T = (L/g)^{1/2}$ is the normalization factor. For these simulations, the non-dimensional time step is t=0.0005. The numerical simulations run 12001 time steps corresponding to 6 ship lengths. They each require 50 hours of wall-clock time.

Figure 1 shows wave cuts for the 10.5 knot case. The correlation coefficients between experimental measurements and numerical predictions for parts (a) thru (d) of Figure 1 are 0.89, 0.91, 0.85, and 0.86, respectively. The solid and dashed lines respectively denote the experimental measurements and the numerical predictions. The correlation gets poorer in the region where the grid spacing along the y-axis gets poorer. The shortest waves are not resolved by the numerical simulations. More grid resolution is required. Convergence studies are in progress.

Figure 2 shows wave cuts for the 18 knot case. The correlation coefficients between experimental measurements and numerical predictions for parts (a) thru (d) of

Figure 2 are 0.89, 0.92, 0.88, and 0.91, respectively. In general, the high Froude-number simulation is in slightly better agreement with the experimental measurements than the low Froude-number simulation, probably because the waves are longer. However, both simulations would benefit from using higher resolution, especially near the bow and transom where there is wave breaking and flow separation.

5415 geometry

Experimental measurements of a DDG model 5415 have been performed at Froude numbers Fr=0.2755 and 0.4136 that correspond to equivalent full-scale speeds of 20 and 30 knots, respectively. The measurements include free-surface profiles on the ship hull, free-surface elevations near the bow and stern using a whisker probe, and total drag. The length, beam, and draft of the model are respectively 5.72m, 0.388m, and 0.248m. The model-scale speeds are 4.01 and 6.02 knots. Details of the hull geometry, including the sinkage and trim, are provided by the Carderock Division (2005).

A three-dimensional numerical simulation using 800x192x192=29,491,200 grid points, 4x8x8=256 subdomains, and 256 nodes has been performed on a Cray XT3. The length, width, depth, and height of the computational domain are respectively 3.0, 1.0, 1.0, 0.5 ship lengths (L). Grid stretching is employed in all directions. The smallest grid spacing is 0.0008L near the ship and mean waterline, and the largest grid spacing is 0.05L in the far field. For the high Froude-number case, this provides about 15 x 100 grid cells across the transom and 1340 grid cells per transverse wavelength (1.07L) where the grid spacing is fine and 20 grid cells where it is coarse. Initial transients are minimized by slowly ramping up the free-stream current. As before, the period of adjustment associated with this ramp up is 0.5 in non-dimensional units of time. For this simulation, the non-dimensional time step is t=0.0002. The numerical simulation runs 28001 time steps corresponding to 5.6 ship lengths. It requires 125 hours of wall-clock time.

Figure 4 compares NFA predictions to experimental measurements for the flow near the bow. The free-surface profile measurements are denoted by spherical symbols along the ship hull. The ship hull is outlined in grey. Whisker-probe measurements are indicated by the small spherical symbols transverse to the ship. Due to the measuring technique, whisker-probe data provides an upper bound of the free-surface elevation. NFA predictions of the free surface are denoted by the color contour. In general, the whisker-probe measurements agree well with the upper bound of the free-surface predictions. NFA correctly predicts the overturning of the bow wave and the resulting splash up slightly aft of the bow. At this resolution, the numerical simulations do not resolve the very thin sheets which characterize the run-up near the bow. As a result, the NFA predictions are slightly lower than the maximum free-surface profile that has been measured.

Figure 3 compares NFA predictions to whisker-probe measurements for the flow near the stern. The portion above the centerline of the ship represents NFA results while the portion below is based on experiments. Black lines mark the edges where spilling occurs. NFA accurately captures the flow separation from the transom stern and agreement between predictions and measurements is good overall. However, at this resolution some spilling along the edges of the rooster tail is not captured. As a result, the predicted rooster-tail amplitude directly astern of the transom is higher than measurements. Simulations that resolve the breaking in this region may provide the dissipation of energy that is necessary to reduce the wave amplitude in the rooster-tail region.

Figure 5 shows transverse cuts of the free-surface elevation near the bow. The cross section of the port side of the hull is outlined using a grey shade. Circular symbols denote the profile measurements along the side of the hull. Solid lines denote whisker-probe measurements. Dashed lines denote NFA predictions. Results are shown for various stations aft of the bow from (a) x=0 to (t) x=-0.169L, where L is the ship length. The figures show the overturning of the bow wave. The initial onset of air entrainment is evident in the NFA predictions. In addition, fragments of splash up are also captured. As expected, the whisker-probe measurements provide an upper envelope to the numerical predictions. This effect is illustrated in Figure 5k, where the bow wave is just beginning to overturn. For this station, there is a sudden jump in the whisker-probe measurement that corresponds to the instrument measuring the top of the spray sheet. The envelop of the plunging event is captured well by the numerical simulations as illustrated in Figures 5k-o. Figures 5o & 5p show the initial stages of splash up. The results of the numerical simulation are not as energetic as the experiments. Higher resolution may help in this particular region. The entrainment of air is observed in Figure 5p-t. The splash up is resolved better by the numerical simulations in Figures 5s & 5t. However, the whisker-probe measurements are consistently lower than the numerical simulations in Figures 5q-t. This requires further study to find the source of the discrepancy.

Figure 6 shows the total resistance as a function of time. Time is normalized by L_o/U_o, where $L_o = 5.72m$ and $U_o = 3.10m/s$. The solid line is the measured steady-state value and the dashed line is the unsteady NFA prediction. The NFA predictions are calculated by integrating the normal component of the pressure along the direction of travel over the surface of the ship hull. Based on ITTC line, the portion of the drag that tangential to the ship is added to these results to predict the total drag. This additional term is required because NFA is

7

an Euler code that does not directly predict skin-friction drag. Unlike potential-flow formulations, NFA does not require a correction for residuary resistance associated with the shedding of vorticity because Euler formulations account for base drag. The figure shows NFA results converging to the steady-state resistance. We note that there are known long-time transients associated with a ship accelerating from rest to constant forward speed (Dommermuth, Sussman, Beck, T.O'Shea, Wyatt, Olson & MacNeice 2004).

Sphere geometry

Consider the motion of a heaving sphere that is moving with forward speed. The purpose of this study is to build toward developing a capability that is suitable for forced-motion studies and seakeeping. The Froude number is $Fr = U_o/\sqrt{gD} = 0.5$, where D is the diameter of the sphere. The normalized diameter of the sphere is $D = 1$. The amplitude of the heaving motion is $A = 0.25$ and the frequency of oscillation is $\omega = 2\pi$ (see Equation 33). Three grid resolutions are studied: $64^3 = 262,144$, $128^3 = 2,097,152$, and $256^3 = 16,777,216$ grid points. The length, width, and height of the computational domain are 4. The smallest grid spacings for the coarse, medium, and fine grids are respectively 0.00412, 0.0206, and 0.0103. The time steps are respectively 0.0025, 0.00125, and 0.0006225.

Figure 7 shows the x-component of force acting on a sphere moving with forward speed, and Figure 8 shows the z-component. The forces are normalized by the displacement of the sphere, which is initially half immersed. The forces only include the portion of the pressure that is directed normal to the surface of the sphere. The effects of skin friction are not included. First- and second-harmonic interactions are evident in both components of force. The second-harmonic interactions are particularly strong for the vertical component of force, probably due to wave breaking and collapse beneath the sphere.

Figure 9 shows a time sequence of a heaving sphere moving with forward speed. The initial start-up stage is shown. A plunging breaker forms near the bow in Figure 9g. Upon breakup, the flow becomes very turbulent.

Conclusions

In terms of progress, it is interesting to consider the results of research reported in earlier ONR symposiums. Dommermuth et al. (1998) study the flow near the bow of model 5415 using a variable-density, cartesian-grid formulation. A body force is used by Dommermuth et al. (1998) to impose the body boundary condition. The numerical results of Dommermuth et al. (1998) barely capture the initial onset of wave overturning near the bow. Sussman & Dommermuth (2001) continue to develop

interface capturing methods. Once again, comparisons are shown to the bow flow of model 5415. The results do not show significant improvement over their earlier results. However, their calculations of the breakup of a turbulent spray sheet illustrate a novel application of interface-capturing methods. Dommermuth et al. (2004) use two methods to study the flow around model 5415, a vertical strut, and a bluff wedge. The first method uses free-slip conditions on the hull in combination with a hybrid level-set and VOF interface-capturing method. In addition, adaptive mesh refinement (AMR) is used to improve grid resolution near the hull and free-surface interface. Their preliminary results illustrate the efficiency of AMR. The second method uses body-force and VOF formulations on a cartesian grid with no grid stretching. The results show more fine-scale detail than the earlier studies. The predicted free-surface elevations compare well with experiments, but the body-force method is too "sticky." Based on these results, the present research uses free-slip boundary conditions to impose the body boundary condition to reduce stickiness. The VOF algorithm has been generalized to include free-slip conditions on the ship hull. The grid is stretched along the cartesian axes to improve grid resolution. Together, these new formulations enable the modeling of complex free-surface flows.

It is not possible to show all of the details in the current numerical predictions through the use of figures. In order to study the flow in even more detail, several animations have been prepared at the flow visualization center at ERDC. The animations are accessible by contacting the authors. Animations are available for all the cases shown in this paper.

References

Carderock Division, Surface Ship Model 5415, Tech. rep., Naval Surface Warfare Center, 2005.
    URL: *http://www.dt.navy.mil/hyd/sur-shi-mod/*

Colella, P., Graves, D., Modiano, D., Puckett, E., & Sussman,

M., "An embedded boundary / volume of fluid method for free-surface flows in irregular geometries," <u>Proceedings of FEDSM99, 3rd ASME/JSME Joint Fluids Engineering Conference</u>, San Francisco, CA., 1999, pp. 0–0.

Dommermuth, D., "The initialization of vortical free-surface flows," <u>J. Fluids Eng.</u>, Vol. 116, 1994, pp. 95–102.

Dommermuth, D., Innis, G., Luth, T., Novikov, E., Schlageter, E., & Talcott, J., "Numerical simulation of bow waves," <u>Proceedings of the 22nd Symposium on Naval Hydrodynamics</u>, Washington, D.C., 1998, pp. 508–521.

Dommermuth, D. G., "The initialization of nonlinear waves using an adjustment scheme," <u>Wave Motion</u>, Vol. 32, 2000, pp. 307–317.

Dommermuth, D. G., Sussman, M., Beck, R. F., T.O'Shea, T., Wyatt, D. C., Olson, K., & MacNeice, P., "The numerical simulation of ship waves using cartesian-grid methods with adaptive mesh refinement," <u>Proceedings of the 25th Symposium on Naval Hydrodynamics</u>, St. John's, Newfoundland and Labrador, Canada, 2004, pp. 0–0.

Gueyffier, D., Li, J., Nadim, A., Scardovelli, R., & Zaleski, S., "Volume-of-fluid interface tracking with smoothed surface stress methods for three-dimensional flows," <u>J. Comp. Phys.</u>, Vol. 152, 1999, pp. 423–456.

Knupp, P. M. & Steinerg, S., <u>Fundamentals of grid generation</u>, CRC Press, Inc., 1993.

Leonard, B., "Bounded higher-order upwind multidimensional finite-volume convection-diffusion algorithms," W. Minkowycz & E. Sparrow, eds., <u>Advances in Numerical Heat Transfer</u>, Taylor and Francis, Washington, D.C., 1997, pp. 1–57.

Mampaey, F. & Xu, Z.-A., "Simulation and experimental validation of mould filling," <u>Modeling of Casting, Welding and Advanced Solidification Processes VII</u>, London, England, 1995, pp. 10–12.

Orlanski, I., "A simple boundary condition for unbounded hyperbolic flows," <u>J. Comp. Phys.</u>, Vol. 21, 1976, pp. 251–269.

Pilliod, J. & Puckett, E., <u>Second-Order Accurate Volume-of-Fluid Algorithms for Tracking Material Interfaces</u>, Technical Report LBNL–40744, Lawrence Berkeley National Laboratory, 1997.

Puckett, E., Almgren, A., Bell, J., Marcus, D., & Rider, W., "A second-order projection method for tracking fluid interfaces in variable density incompressible flows," <u>J. Comp. Physics</u>, Vol. 130, 1997, pp. 269–282.

Repetto, R. A., <u>Computation of turbulent free-surface flows around ships and floating bodies</u>, Ph.D. thesis, Technischen Universität Hamburg-Harburg, 2000.

Rider, W., Kothe, D., Mosso, S., Cerutti, J., & Hochstein, J.,

"Accurate solution algorithms for incompressible multiphase flows," <u>AIAA paper 95–0699</u>.

Sussman, M., "A second order coupled level set and volume-of-fluid method for computing growth and collapse of vapor bubbles," <u>J. Comp. Phys.</u>, Vol. 187, 2003a, pp. 110–136.

Sussman, M. & Dommermuth, D., "The numerical simulation of ship waves using cartesian-grid methods," <u>Proceedings of the 23rd Symposium on Naval Ship Hydrodynamics</u>, Nantes, France, 2001, pp. 762–779.

Wilson, W., Fu, T., Pence, A., & Gorski, J., "The measured and predicted wave field of model 5365: an evaluation of current cfd capability," <u>Proceedings of the 26th Symposium on Naval Hydrodynamics</u>, Rome, Italy, 2006, pp. 0–0.
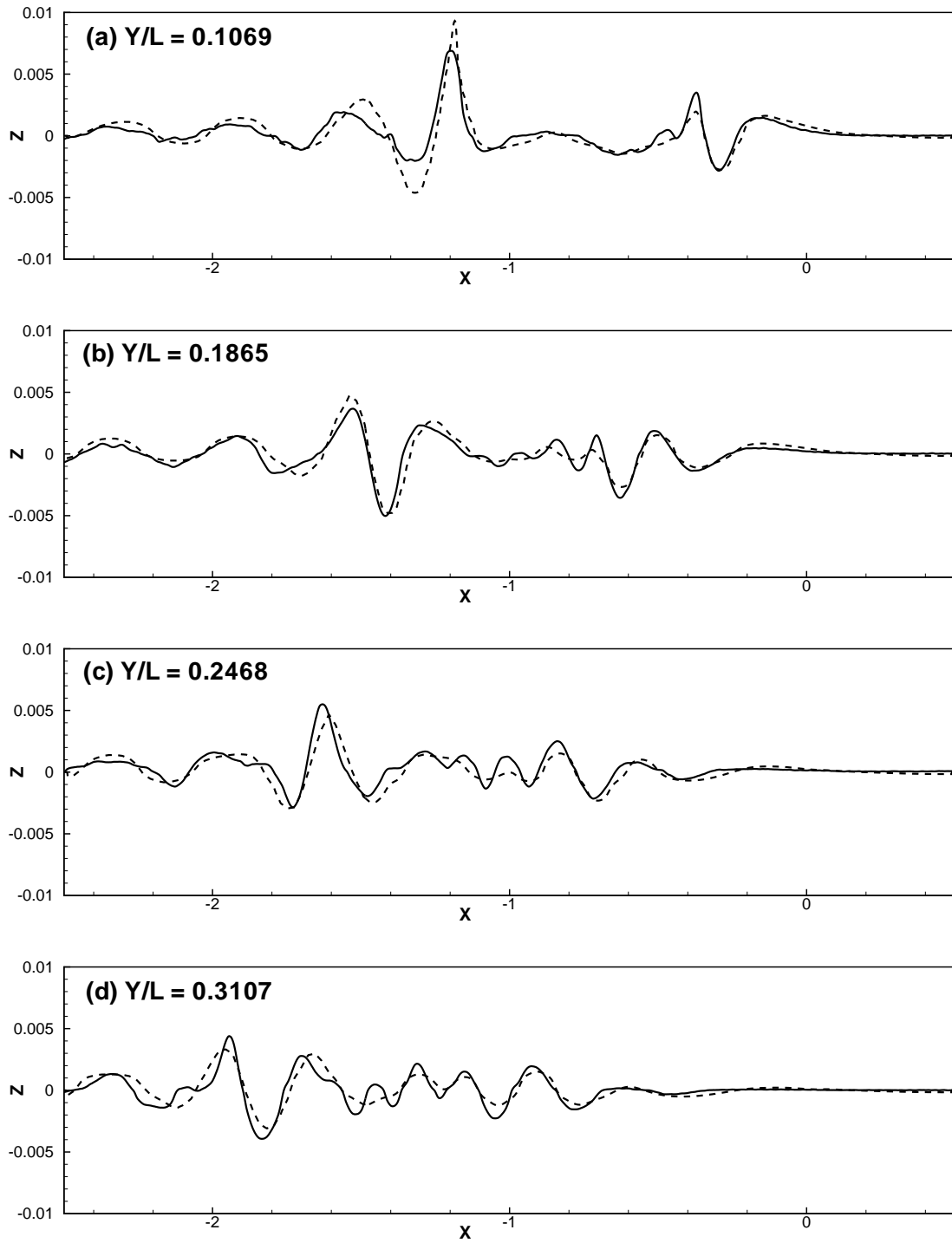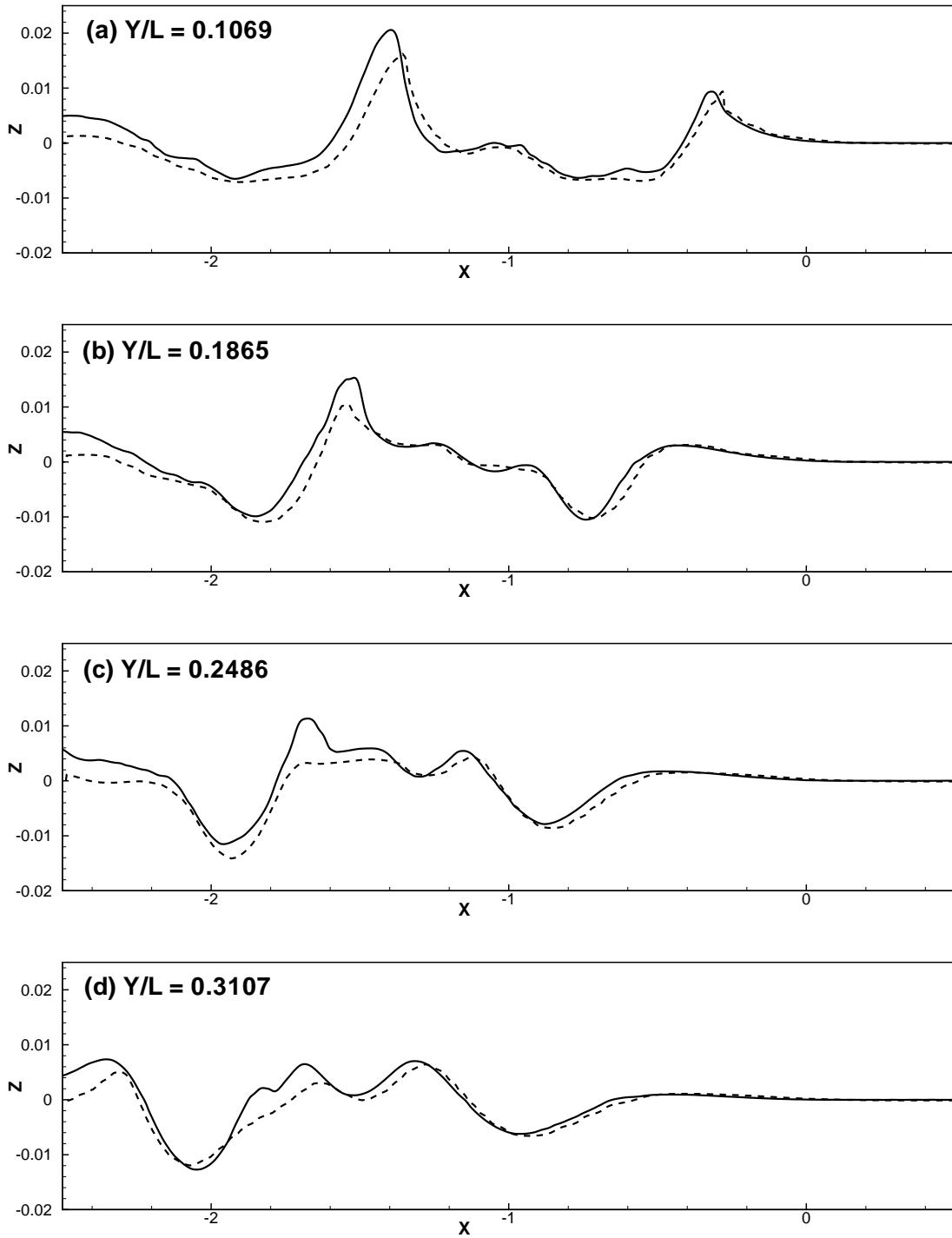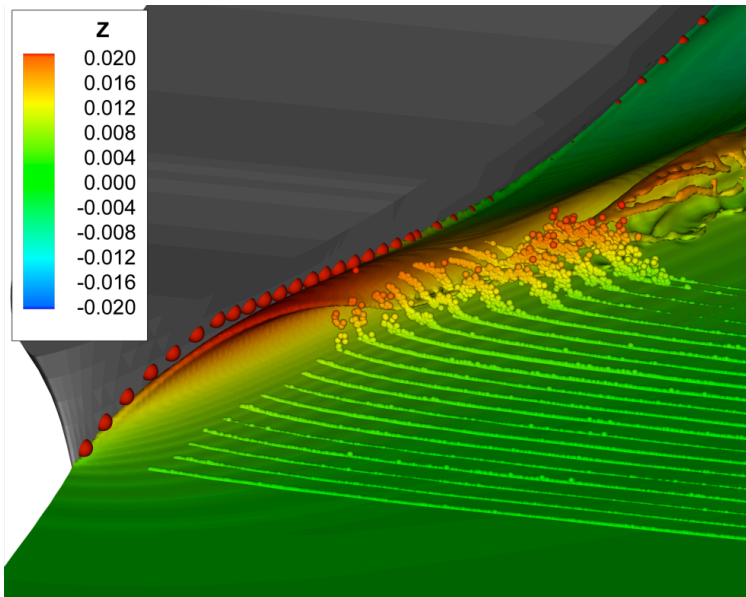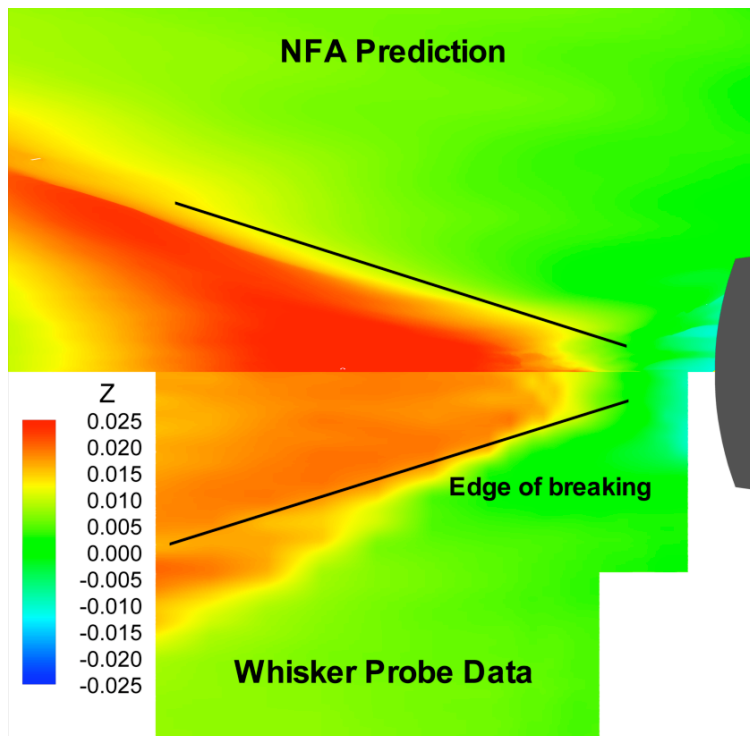
Figure 1: Athena 10.5 knot wave cuts.

Figure 2: Athena 18 knot wave cuts.

Figure 3: Model 5415 bow view.
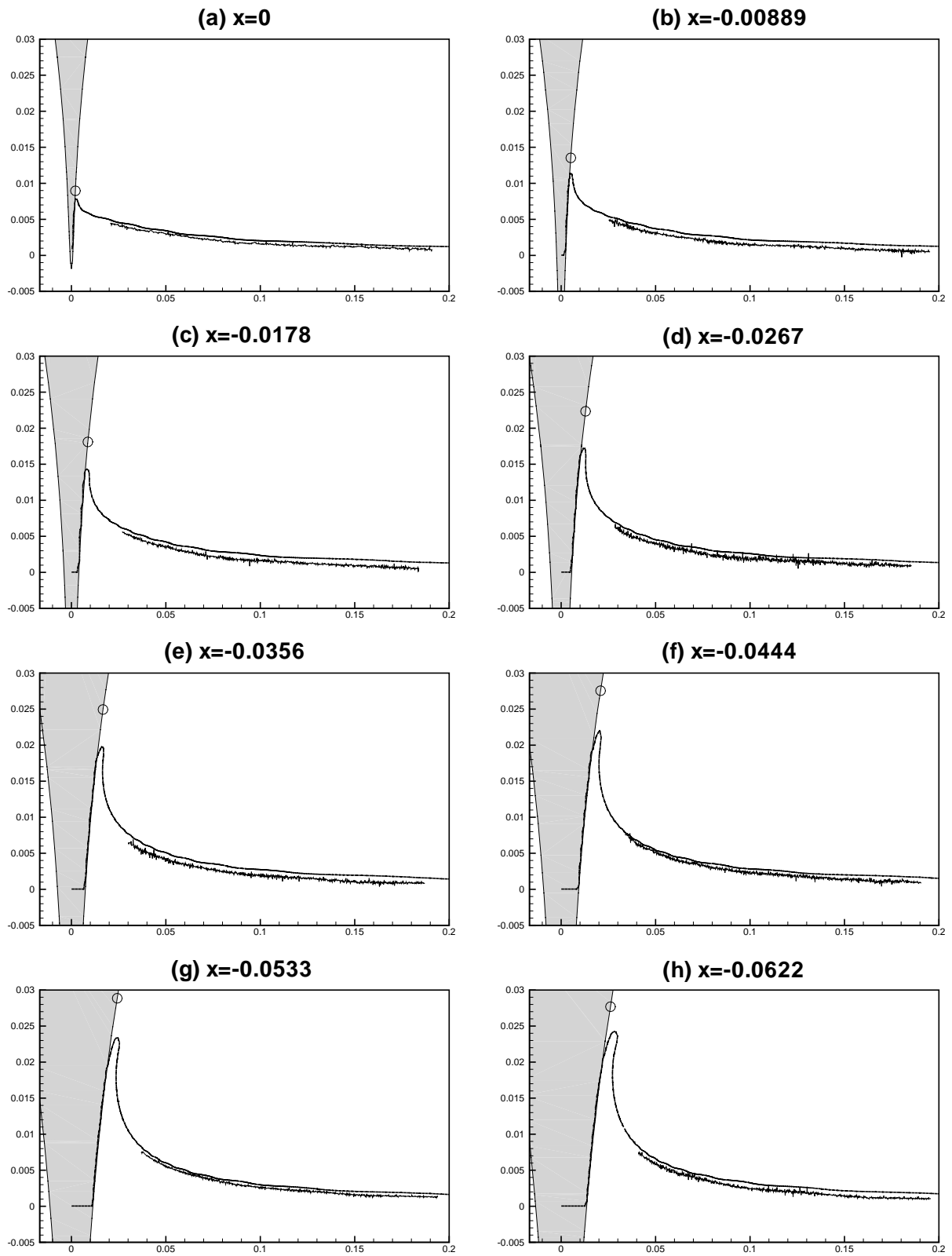

Figure 4: Model 5415 stern view.
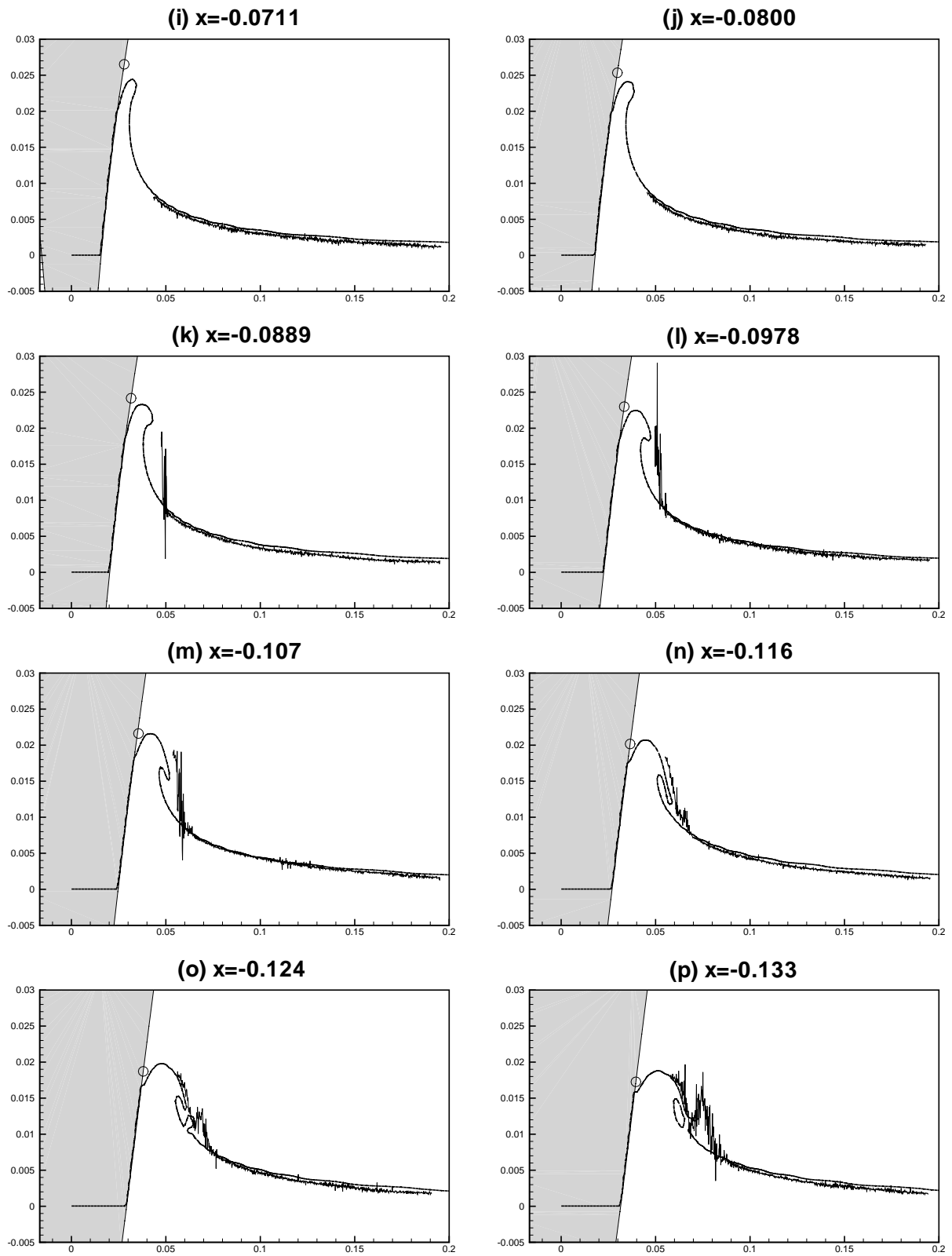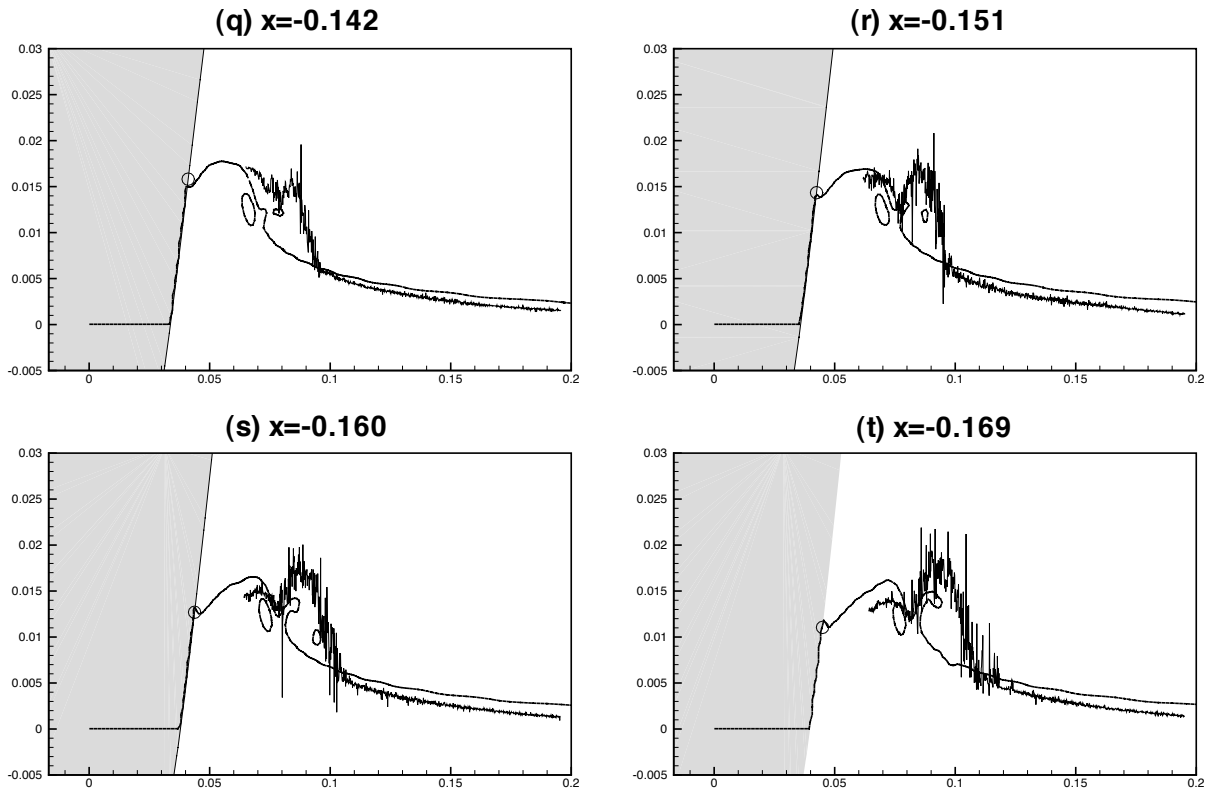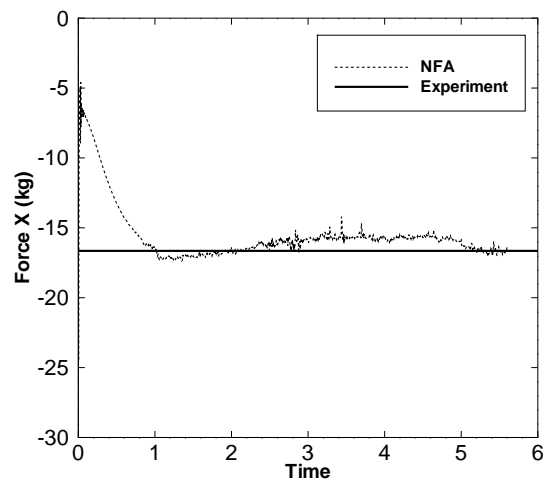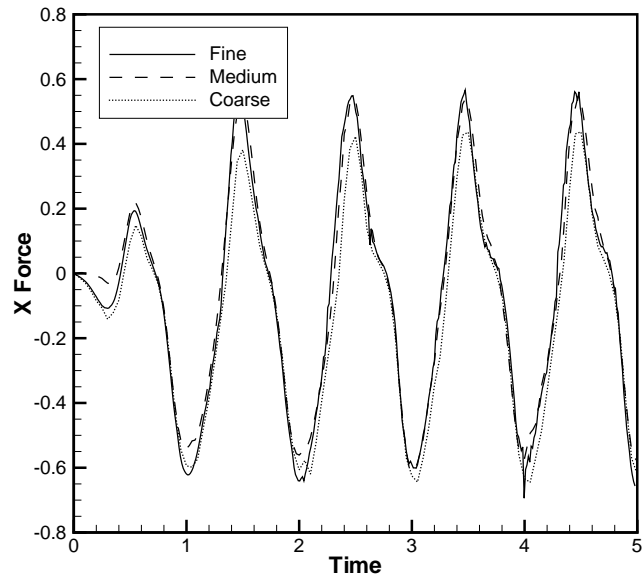
Figure 5: Model 5415 transverse wave cuts.

(i) x=-0.0711

(j) x=-0.0800

(k) x=-0.0889

(l) x=-0.0978

(m) x=-0.107

(n) x=-0.116

(o) x=-0.124

(p) x=-0.133

Figure 5: Model 5415 transverse wave cuts, continued.

(q) x=-0.142   **(r) x=-0.151**
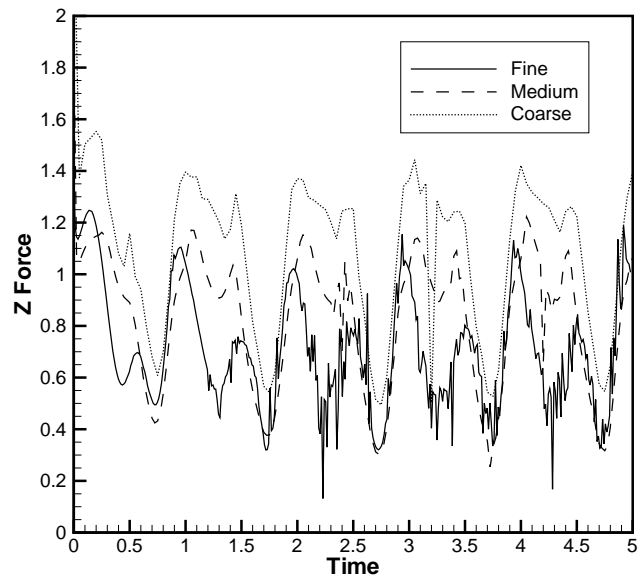
(s) x=-0.160   **(t) x=-0.169**

Figure 5: Model 5415 transverse wave cuts, continued

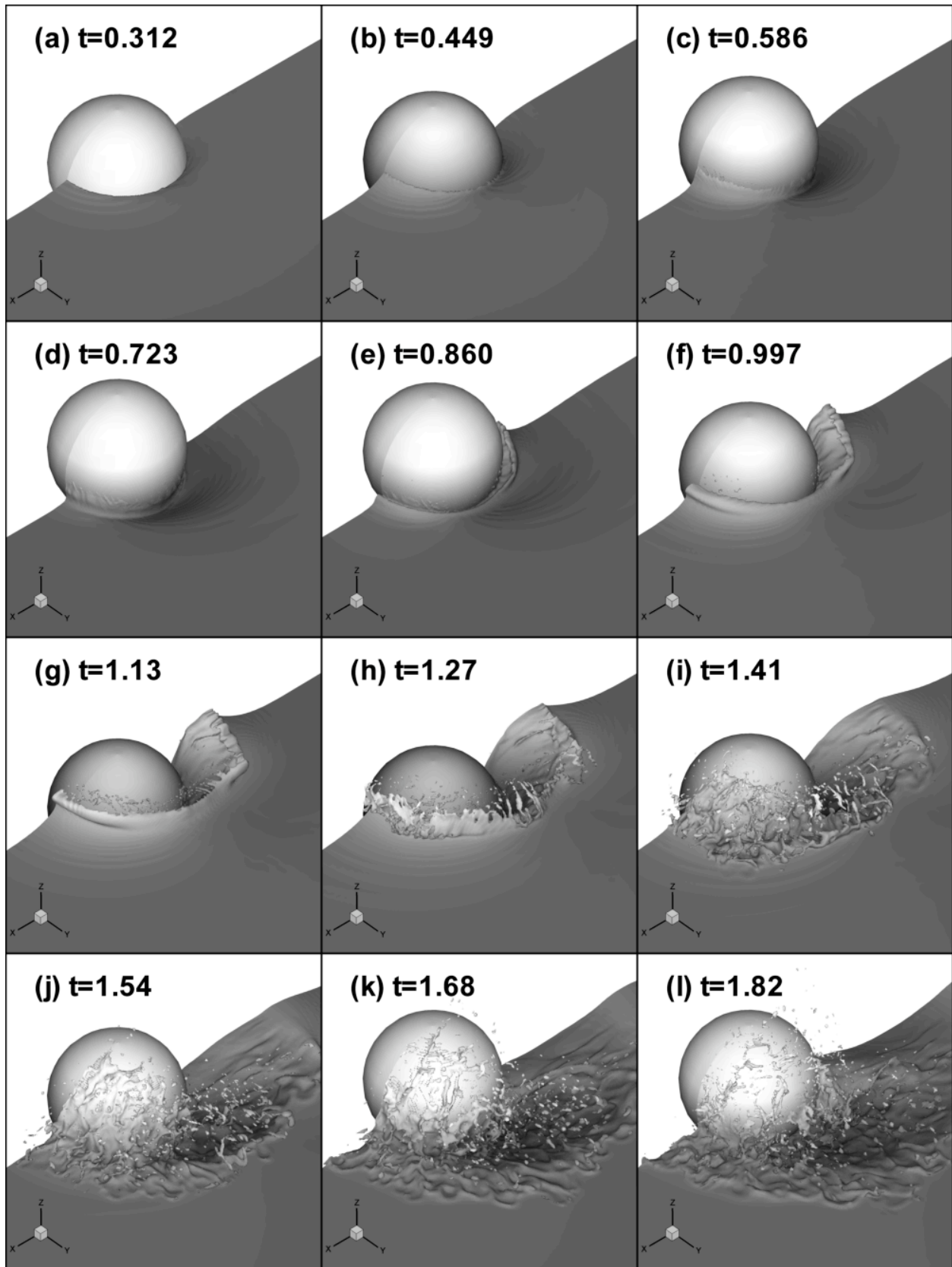**Figure 6:** Model 5415 resistance.

Figure 7: X-component of force acting on a heaving sphere moving with forward speed.

Figure 8: Z-component of force acting on a heaving sphere moving with forward speed.

Figure 9: Time sequence of a heaving sphere moving with forward speed.